

**The impact of subsampling on MODIS Level-3 statistics of cloud optical
thickness and effective radius**

Lazaros Oreopoulos

Joint Center for Earth Systems Technology, University of Maryland Baltimore County

and

Laboratory for Atmospheres, NASA-Goddard Space Flight Center

Revised for IEEE Transactions on Geosciences and Remote Sensing

October 2004

Abstract

The MODIS Level-3 optical thickness and effective radius cloud product is a gridded $1^\circ \times 1^\circ$ dataset that is derived from aggregation and subsampling of every 5th pixel, along both spatial directions, of Level-2 orbital swath data (Level-2 granules). The present study examines the impact of this subsampling on the mean, standard deviation and inhomogeneity parameter statistics of optical thickness and effective radius. The methodology is simple and consists of estimating mean errors for a large collection of Terra and Aqua Level-2 granules by taking the difference of the statistics at the original and subsampled resolutions. It is shown that the Level-3 subsampling does not affect the various quantities investigated to the same degree, with second order moments suffering greater subsampling errors, as expected. Mean errors drop dramatically when averages over a sufficient number of regions (e.g., monthly and/or zonal averages) are taken, pointing to a dominance of errors that are of random nature. When histograms built from subsampled data with the same binning rules as in the Level-3 dataset are used to reconstruct the quantities of interest, the mean errors do not deteriorate significantly. The results in this paper provide guidance to users of MODIS Level-3 optical thickness and effective radius cloud products on the range of errors due to subsampling they should expect and perhaps account for, in scientific work with this dataset. In general, subsampling errors should not be a serious concern when moderate temporal (e.g., monthly) and/or spatial (e.g., zonal) averaging is performed.

I. Introduction

In order to study the global distribution of cloud properties and the main features of their monthly, seasonal and diurnal evolution, in other words, in order to examine cloud climatology, a gridded set of spatially-averaged cloud retrievals would be the most convenient. Such a product is provided for the MODIS instrument aboard the EOS Terra and Aqua platforms as Level-3 MOD08* (Terra) and MYD08* (Aqua) datasets [1]. There are actually three Level-3 MODIS cloud products available for each platform. Statistics are summarized over a $1^\circ \times 1^\circ$ global grid for daily (D3), eight-day (E3), and monthly (M3) time scales. Each of the Level-3 products contain statistics generated from the Level-2 (Orbital Swath) products. Statistics for a given derived quantity or Science DataSet (SDS) might include: simple (mean, minimum, maximum, standard deviation) statistics; parameters of normal and lognormal distributions; fraction of pixels that satisfy some condition (e.g. cloudy, clear); histograms of the quantity within each gridpoint; histograms of the confidence placed in the retrieved quantity; histograms and/or regressions derived from comparing one science parameter to another; statistics computed for a subset that satisfies some condition [1]. All these statistics are computed by subsampling pixel-level values of 1 km nadir resolution every 5th pixel, along both spatial directions, since the geolocation internal to the MOD06 (Level-2) cloud product is 5 km [1]. Thus, cloud optical thickness or effective radius statistics for an overcast $1^\circ \times 1^\circ$ gridpoint around the equator that contains pixels observed at near-nadir view angles, come from about ~480 pixels instead of the ~12,000 1-km pixels that are originally contained within the gridpoint. The subject of this study is to examine whether the process of subsampling has distorting effects on several Level-3 SDSs and other

quantities of interest derived from them. This is obviously an important issue for current and future users of the Level-3 cloud dataset who intend to compare MODIS cloud climatologies with those from other sources.

The outline of the paper is as follows: First, we present in section II the dataset used to examine the subsampling effect, the SDSs and other quantities we are interested in, and discuss the methodology for analyzing the subsampling errors. In section III we present results for optical thickness statistics, and in section IV for effective radius statistics. Section V, examines whether the findings in sections III and IV are affected when the quantities of interest are derived from histograms built following Level-3 binning rules for optical thickness and effective radius. The final section consists of an overview discussion on our findings and their implications for users of MODIS Level-3 cloud climatologies.

II. Dataset and methodology

We use 300 Level-2 granules, each consisting of 2030 pixels along track and 1354 pixels across track, obtained for various post-2000 November months for both Terra (200 granules) and Aqua (100 granules). The granules are largely confined within 20°N to 60°N (with most granule centers falling within 20°N and 50°N), while covering the full meridional range. They contain a wide variety of cloud scenes with different phases, cloud fraction, thickness and degree of inhomogeneity. For those pixels identified as cloudy from the cloud masking algorithm [2], the cloud phase is determined (“liquid”, “ice”, “undetermined”) and subsequently cloud optical thickness, τ , and cloud effective radius, r_{eff} , (ratio of the third to the second moment of the cloud particle radius

distribution) is retrieved (among others) [3]. The retrievals used here come from the $0.65\ \mu\text{m}$ (over land) and $0.86\ \mu\text{m}$ (over ocean) bands that are the most sensitive to changes in cloud optical thickness, in conjunction with the $2.1\ \mu\text{m}$ band which is most sensitive to changes in cloud particle size [3]. The resolution of these retrievals (pixel size) is 1 km for near-nadir observations, but decreases gradually (pixel size increases) with view angle [4]. In this study, the pixel-by-pixel phase determination for our dataset will be largely ignored since it is not an essential factor in subsampling error estimates as will become evident later. The only instance where phase enters the discussion is in section V where, due to different histogram binning rules for the two phases, *all* cloudy pixels are assumed to be of one or the other phase.

In the Level-3 dataset, the statistics of each $1^\circ \times 1^\circ$ gridpoint (near the equator) are derived by subsampling and aggregating every 5th of approximately 110×110 pixels near-nadir (1 km resolution). However, the available number of pixels to be subsampled approximately decreases with the cosine of latitude as one moves poleward. For example, at $\sim 83^\circ$, each $1^\circ \times 1^\circ$ gridpoint is made of ~ 1600 1 km pixels. At the same time, for observations close to the edge of the orbital swath, due to pixel expansion, fewer pixels are needed to cover a $1^\circ \times 1^\circ$ geographic area (an effect somewhat compensated by accompanying pixel overlap, [4]). Thus, the number of pixels used to construct the Level-3 statistics can potentially become quite small, especially when only a fraction of the gridpoint is cloudy (as is often the case). The impact of the varying number of pixels used to construct Level-3 statistics has to be therefore taken into account in the analysis.

The approach used in this work is the following: The granules are divided into 110×110 , $100 \times 100 \dots 40 \times 40$ pixel regions (i.e., 8 regions sizes). Since one of the main

goals is to examine the effects of subsampling on the cloud optical thickness inhomogeneity climatology presented in the paper by Oreopoulos and Cahalan [5], only regions with cloud fraction (fraction of pixels with non-zero optical thickness) greater than 0.1 are considered, as in that work. For each of these regions (e.g. ~53,000 regions of 110x110 pixels), and for the optical thickness part of the analysis, cloud fraction (CF), spatial mean of optical thickness $\bar{\tau}$, standard deviation of optical thickness σ_τ , and the inhomogeneity parameters

$$v_{MOM} = \left(\frac{\bar{\tau}}{\sigma_\tau} \right)^2 \quad (1a)$$

$$v_{MLE} = \frac{1 + \sqrt{1 + 4y/3}}{4y} \quad (1b)$$

$$\chi = \frac{e^{\overline{\ln \tau}}}{\bar{\tau}} \quad 0 < \chi \leq 1 \quad (1c)$$

are calculated. In eq. (1b), $y = \ln \bar{\tau} - \overline{\ln \tau}$. The first two equations provide two different ways to estimate the shape parameter of a gamma distribution which has been found to describe well observed distributions of cloud optical thickness [6], [7]. The first equation is for the Method Of Moments (MOM), and the second is an empirical approximation for the Maximum Likelihood Estimate (MLE) method which gives a shape parameter less sensitive to outliers [8]. The third equation is the definition of the inhomogeneity parameter of Cahalan *et al.* [9] which approximates the factor by which $\bar{\tau}$ should be multiplied to recover the mean albedo of a region. For the effective radius part of the analysis, the mean and standard deviation of effective radius are calculated.

For both optical thickness and effective radius two methods of calculation are used: 1) all the cloudy pixels within the region are included; and 2) only every 5th pixel along both spatial directions, if it happens to be cloudy, is included. The percentage difference of the values obtained from the above two methods gives the impact of subsampling as a percentage error (positive signifies that subsampling underestimates). Cloud phase is ignored in this procedure, so the means and standard deviations obtained closely correspond to their counterpart SDSs for “Combined Optical Thickness” and “Combined Effective Radius” in the Level-3 MODIS products.

The analysis shown in the following also accounts for the fact that, at most times, we are not interested in the error of a single region, but in the error of an ensemble of regions. For example, in the work by Oreopoulos and Cahalan [5] the authors are interested in the climatology of χ and ν , so they examine monthly, zonal, and global averages of these quantities. The mean error of an ensemble of 30 regions can then be thought of as the mean monthly sampling error for a single 1°x1° gridpoint. Similarly, the error for an ensemble of 90 regions can be thought of as the mean seasonal sampling error of a single gridpoint, the error of an ensemble of 360 regions as the mean annual sampling error of a single gridpoint or the daily error of a latitude zone, and the error for an ensemble of 10,000 regions (~30x360) as the mean monthly subsampling error of a latitude zone. To examine these “climatological” errors, 1000 ensembles of regions are constructed with each ensemble resulting from assembling in a random fashion, a prespecified number of regions (1, 30, 90, 360, 10,000) for each of the 8 region sizes, so that 5000 ensembles correspond to each region size, i.e., 1000 consisting of 1 region, 1000 consisting of 30 regions, etc. The distribution of errors for these 40,000 ensembles

can then be examined. The random fashion with which the ensembles are built also ensures that regions observed under a variety of viewing angles are combined, thus crudely simulating the fact that over a period of time each $1^\circ \times 1^\circ$ gridpoint contains pixels viewed under a wide range of scan angles (a similar argument applies for gridpoints that make up a latitude zone). Still, it is not clear that pixel expansion at large view angles systematically increases the subsampling errors. Indeed, when regions consisting of the same number of pixels, but viewed at near-nadir and the largest view angles (i.e., larger regions at the edges of the swath) were compared with respect to subsampling errors, they were not substantially different. This may be because pixel expansion with view angle is accompanied by simultaneous pixel overlap [4] which tends to reduce subsampling effects.

III. Optical thickness errors

Figure 1 shows the errors of subsampling (in %) of $\bar{\tau}$ and σ_τ for all ($\sim 53,700$) 110×110 regions of our dataset (except for those few whose errors fall outside the $\pm 50\%$ bounds of the plot). Errors for individual regions are often quite large, although the greatest concentration of points is within the $\pm 20\%$ error bounds. There is about the same number of regions with positive and negative errors in $\bar{\tau}$, and the same applies for σ_τ . This is a good indication of the random nature of these errors. For most regions ($\sim 76.6\%$ of the regions) overestimates in $\bar{\tau}$ by subsampling are accompanied by overestimates in σ_τ and vice-versa (upper-right and lower-left quadrants), but the number of regions where the error is of opposite sign is still substantial. The top panel of Fig. 2 shows a similar graph, but this time for CF and χ . The errors in this case are generally smaller with the densest

concentration of points confined within the $\pm 10\%$ error bounds. The number of regions on each quadrant is now distributed more evenly than in the previous figure. The bottom panel shows the % errors in χ for each region as a function of the cloud fraction of the region before subsampling, and indicates that the distribution of χ errors tightens around smaller values as cloud fraction increases.

Figure 3 shows the mean error for 110x110 pixel regions as a function of cloud fraction. Each value was obtained by averaging the errors of regions that have cloud fraction within the predetermined 0.1-width bin. Note that the last bin has by far the most values consistent with the well-known *U*-shape behavior of cloud fraction distributions. This figure shows prominently the dramatic effect of averaging a large number of random errors: the mean errors of ensembles of $\sim 5,000$ regions and above are very small, with the exception of v_{MOM} at small cloud fractions. The larger impact of sampling on v_{MOM} compared to the other two inhomogeneity parameters can be easily explained: both χ and v_{MLE} depend on first moment quantities (the linear mean and the mean logarithm of optical thickness, the former being simply the ratio $\exp(\overline{\ln \tau})/\bar{\tau}$, and the latter being a function of the difference $\ln \bar{\tau} - \overline{\ln \tau}$), while v_{MOM} depends on a second moment quantity (σ_τ) which is more sensitive to subsampling. Between v_{MLE} and χ , the latter is less affected by subsampling. There are two reasons for this. First, χ is defined simply as the ratio of two quantities while v_{MLE} is a more intricate function of the linear mean and mean logarithm difference (eq. 1b), and is therefore subject to greater error propagation. Second, χ has an upper bound of 1, by definition, while v_{MLE} (and, of course, v_{MOM}) are unbounded. Despite the fact that regions with v_{MLE} or v_{MOM} greater than 40 are excluded

in the analysis to eliminate contributions from pathological cases, some residual impact from regions with large v_{MOM} , where its value can be easily affected by subsampling, remains. Thus, the unbounded nature of v_{MOM} is responsible for the apparent paradox that some of the most homogeneous regions can also potentially be the ones suffering from the greatest percentage subsampling errors for this particular parameter.

Further evidence of the beneficial effects of averaging errors over a group of regions is shown in Fig. 4. These percentage errors of χ and v_{MLE} are for 1000 ensembles each consisting of 30- and 10,000- regions. The size of each region in these randomly constructed ensembles is 110x110 pixels. As discussed in section 2, the mean error of an ensemble of 30 regions is meant to represent typical monthly average errors of individual gridpoints, while the mean error of an ensemble of 10,000 regions approximates typical monthly-average errors of latitude zones. The mean error of 30-region ensembles almost always stays within $\pm 2\%$ for χ and within $\pm 10\%$ for v_{MLE} . The mean errors of ensembles consisting of 10,000 regions are much smaller than the 30-region ensembles and cluster within a very small range of values. The clustering is not surprising since each of the 10,000-region ensembles, even if constructed randomly, contains many common regions with the other ensembles because the population from which it is drawn is only larger by an approximate factor of 5 (there are $\sim 53,700$ 110x110 regions in the dataset). It is also interesting that the mean errors of 10,000-region ensembles are always positive for χ . This is because of the tight range of χ errors and the fact that a slightly larger number of regions with positive errors exists (Fig. 2, top, indicates that 52.7% of regions have positive errors). On the other hand, because of the wider range of v_{MLE} errors, there are

both positive and negative mean errors for 10,000-region ensembles. The positives dominate due to the larger fraction of positive errors for individual regions ($\sim 55\%$).

Another way to assess the errors of subsampling on optical thickness statistics is shown in Fig. 5. The top panel shows the bounds of percentage errors that contain 95% of the 1000 ensembles, for ensembles consisting of various region numbers (each of 110x110 pixel size) as indicated in the abscissa. For example, the top panel of Fig. 5 indicates that 95% (950) of 90-region ensembles have mean errors of v_{MOM} within $\pm 5.2\%$ (3rd point of topmost curve). CF and χ have the smallest error bounds that contain 95% of the ensembles, followed by $\bar{\tau}$, v_{MLE} , and v_{MOM} . For ensembles consisting of 10,000 regions the error range that contains 95% of the ensembles is smaller than $\pm 2\%$ for all quantities ($\pm 0.25\%$ for χ). The bottom panel of Fig. 5 shows the percentage error range that contains 95% of 30-region ensembles of region size indicated in the abscissa. For example, 95% of 30-region ensembles have v_{MOM} subsampling errors within $\pm 12.95\%$ when the region size is 60x60 pixels (third point of topmost curve). Because the number of ensembles is kept constant at 1000 for each region size (even if more regions of smaller size actually exist in the dataset), it is not surprising that there is a tendency for the error range that contains 95% of the ensembles to decrease with region size. In other words, subsampling errors are expected to grow for regions consisting of a smaller number of cloudy pixels (i.e., $1^\circ \times 1^\circ$ gridpoints at higher latitudes, gridpoints containing many edge-of-swath pixels, or gridpoints with smaller cloud fractions).

Finally, one must note that the errors discussed in this section (as well as in the next two sections) for small region sizes (high latitudes) may in some cases actually be overestimates of the errors resulting from the actual Level-3 processing. The reason is

that the number of pixels falling within a $1^\circ \times 1^\circ$ gridpoint each day is greater than that from a single orbital swath. This is because of the overlap of successive Terra and Aqua orbits (except near the equator), which becomes especially pronounced at high latitudes. Hence, the drastic reduction with latitude of the number of pixels contained in $1^\circ \times 1^\circ$ gridpoints is to some extent compensated by repeated sampling of the region as it is being covered by multiple satellite passes.

IV. Effective radius errors

The analysis in this section follows on the footsteps of the analysis in the previous section. Case in point, Fig. 6 is the counterpart of Fig. 1, i.e., it shows the errors for all 110×110 pixel regions, but this time for the mean and standard deviation of effective radius. There are similarities with Fig. 1, such as the rapid decrease in the density of points outside the $\pm 20\%$ error range, but also differences such as the stronger dominance of positive errors for both the mean and the standard deviation. Indeed, only 21.3% of 110×110 regions have negative errors in the mean, and 33.3% have negative errors in the standard deviation. This explains the lack of negative errors when averaging is performed over a larger number of regions, as in Fig. 7 and 8. These show (similar to their counterpart Figs. 3 and 4) the mean error of effective radius mean and standard deviation for 110×110 pixel regions falling within different cloud fraction bins (Fig. 7) and the mean errors of 1000 ensembles of 30 or 10,000 110×110 pixel regions as a function of the corresponding perfectly sampled quantity (Fig. 8). Fig. 7 suggests that mean errors of subsampling for mean effective radius are slightly greater than those for mean optical thickness, while somewhat unexpectedly the error in standard deviation does not improve

with cloud fraction; it does however improve with region size as shown in the bottom panel of Fig. 9 which is analogous to Fig. 5, showing the error range containing 95% of the ensembles. Also, there seems to be resistance in reducing the mean errors below 2% even when ensembles consist of 10,000 regions (Fig. 8, and top panel of Fig. 9).

All the above points to systematic biases in the statistics of effective radius when subsampling is performed: apparently, subsampling yields frequent systematic underestimates of both the mean and the standard deviation of effective radius, i.e., errors are not always random. This curious phenomenon was further explored by examining effective radius histograms retrieved from perfectly-sampled and subsampled data. When the collective (i.e., from all 300 granules) normalized frequency distributions of combined effective radius (i.e., both liquid and ice clouds) were plotted with a $1\ \mu\text{m}$ bin resolution (not shown), there were small but noticeable differences between the histograms: a larger normalized frequency at small effective radii and a smaller at large effective radii occurred for the subsampled retrievals. These differences were large enough to result in systematically smaller effective radii for the subsampled data in the majority of regions to which we divide the granules. They also resulted in somewhat narrower histograms for the subsampled data which explains the tendency for positive subsampling errors in standard deviation. When the histogram analysis was repeated separately for the Terra and Aqua granules, histogram differences appeared only for the Terra platform (incidentally, subsampled and perfectly-sampled histograms of optical thickness were virtually indistinguishable for both platforms). When Terra effective radius histograms were then constructed separately (not shown) for retrievals corresponding to different pairs of detector elements (the $2.1\ \mu\text{m}$ band has 20 detector

elements each of 500 m resolution for a total viewing path of 10 km along track, so for the 1 km effective radius Level-2 product, measurements from 2 detectors are aggregated), one of the histograms stood out as having characteristics such as those described above for the ensemble histogram of subsampled data. This histogram was from the detector pair that yielded lines 1, 11, 21, 31, etc. of the granule which are included in the subsampled dataset of this analysis as well as the actual MODIS Level-3 processing. Thus, bias errors can appear in subsampled Level-3 data if pixel lines with distinct radiative characteristics (and therefore distinct retrieved values) than the other lines are systematically selected by the subsampling algorithm. This is exactly what occurred in this case, and while the bias errors were small in magnitude, they were still easily detected by the subsampling analysis.

V. Errors from histograms

The MODIS Level-3 cloud product also includes SDSs that are histograms of cloud optical thickness and effective radius. These are also constructed from subsampled data. Although the statistical quantities and parameters examined here are either given directly as distinct SDS products ($\bar{\tau}$, σ_{τ} , $\overline{\ln \tau}$) or can be trivially derived from them using eq. (1) (χ , v_{MOM} , v_{MLE}), it would be interesting to obtain an assessment of the errors when the same quantities are calculated from the histogram SDSs.

The three moments, $\bar{\tau}$, σ_{τ} , $\overline{\ln \tau}$, that are needed for eq. (1) are derived from the discrete probability distribution $p(\tau)$ built from the histograms for each region (of the 8 regions sizes) using values subsampled every 5th pixel as follows:

$$\bar{\tau} = \sum_{i=1}^N \tau_i p(\tau_i) \quad (2a)$$

$$\sigma_{\tau} = \left(\sum_{i=1}^N (\tau_i - \bar{\tau})^2 p(\tau_i) \right)^{1/2} \quad (2b)$$

$$\overline{\ln \tau} = \sum_{i=1}^N \ln \tau_i p(\tau_i) \quad (2c)$$

Equations analogous to (2a) and (2b) apply for effective radius mean and standard deviation. The number of bins N varies according to the type of histogram, and the values used for each case will be given below. It should be underlined that the subsampling error is defined in this case as the difference between the value of the desired quantity calculated from the perfectly-sampled data directly (i.e., *not* from histograms constructed from perfectly-sampled data) and the value derived using eq. (2) and histograms built from data subsampled every 5th pixel along both spatial directions.

Figure 10 shows optical thickness results and is the counterpart of the bottom panel of Fig. 5. The top panel is for calculations using MODIS Level-3 binning for liquid clouds ($N = 45$ bins) and the bottom is for calculations using ice cloud binning ($N = 30$ bins). Both histograms extend up to a value of 100 for optical thickness, but the width of the bins is different (the ice histograms better resolve small values of optical thickness and use coarser binning for large values). Results for both panels of Fig. 10 look similar to the results in the bottom panel of Fig. 5, except for the v_{MLE} error with liquid cloud histogram binning which is worse for most region sizes from its counterpart v_{MOM} .

Figure 11 is for effective radius and is the counterpart of the bottom panel of Fig. 9. The top panel is for calculations using histogram binning for liquid clouds and the bottom

is for calculations with ice cloud binning. The former originally uses $N=23$ bins in the Level-3 dataset, extending from 2 to 30 μm , but a 24th very wide bin was added from 30 to 60 μm to accommodate the large particle effective radii encountered in the current dataset. The latter uses $N=12$ histogram bins extending from 6 to 60 μm . Again, there is little difference from what has already been shown in Fig. 9, with the exception of the error in standard deviation when the liquid cloud histogram binning is used. This is probably the result of the coarse last bin that was arbitrarily added. Results with ice cloud binning do not seem to be much affected by omission of particle sizes below 6 μm .

In conclusion, for monthly or longer time scales, one can reconstruct cloud optical thickness or effective radius moments and optical thickness inhomogeneity parameters from MODIS Level-3 histograms (built from data subsampled every 5th pixel) for a $1^\circ \times 1^\circ$ region, without suffering much additional subsampling error relative to the case where the moments and parameters come from distinct Level-3 SDSs.

VI. Summary and conclusions

Cloud optical thickness and effective radius Scientific Datasets (SDSs) in the MODIS Level-3 daily, eight-day, and monthly products come from aggregation on a $1^\circ \times 1^\circ$ grid of Level-2 orbital swath data that have been subsampled every 5th pixel along both spatial directions (along and across the satellite track). The present study examined the impact of this subsampling on cloud fraction, the mean and standard deviation of optical thickness and effective radius, as well as on parameters that convey the radiative impact of optical thickness variability. The subsampling effect was quantified as the percentage difference between perfectly-sampled and subsampled results for ensembles of regions with size on

the order of $1^\circ \times 1^\circ$. The perfectly-sampled data come from 300 Terra and Aqua granules obtained at northern subtropics/midlatitudes for several post-2000 November days.

It was shown that Level-3 subsampling does not affect the various quantities investigated to the same degree, with second order moments and quantities depending on second order moments suffering greater subsampling errors, as expected. For individual regions consisting of 110×110 pixels (about $1^\circ \times 1^\circ$ around the equator) the vast majority of regions have errors within $\pm 20\%$ for mean and standard deviation of optical thickness and effective radius. Errors for cloud fraction and the inhomogeneity parameter χ are smaller, and errors for the inhomogeneity parameters v_{MOM} and v_{MLE} are greater (especially for v_{MOM}). Mean errors drop dramatically when averages over a sufficient number of regions (e.g., monthly and/or zonal averages) are taken: for ensembles of 30 regions (corresponding to monthly averages) errors for most regions sizes are less than 15% for v_{MOM} and v_{MLE} 95% of the time, while for the other quantities they are generally below 5%. Subsampling errors seem to be mostly of random nature, but evidence was found of small but systematic underestimates for effective radius mean and standard deviation. This was traced back to systematic differences in the retrievals from different $2.1 \mu\text{m}$ band detectors: the subsampling procedure was systematically picking a pixel line (from the first two detectors) with radiatively different appearance from the other pixel lines; this pixel line is used in the actual MODIS Level-3 aggregation and subsampling algorithm. Finally, when histograms built from subsampled data with the same binning rules as in the Level-3 dataset are used to reconstruct the quantities of interest, the mean errors at monthly scales do not deteriorate significantly.

It may be worth mentioning that subsampling error analysis was also performed with the 2D bounded cascade model of Cahalan [10] which offers the advantage that the properties of clouds (cloud fraction, degree of inhomogeneity, mean optical thickness) can be easily controlled. Optical thickness errors due to subsampling from MODIS largely mirrored those derived from the model clouds. The ranking of parameters according to error magnitude was the same (χ exhibited the smallest errors and v_{MOM} the largest), the error decreased with cloud fraction and cloud homogeneity, and experienced rapid decline when averaged over ensembles of randomly generated cascade fields.

The results in this paper provide guidance to users of MODIS Level-3 cloud products on the range of errors due to subsampling they should expect and perhaps account for, in scientific work with this dataset. Although the findings do not come from a global dataset of successive satellite orbits which would allow the Level-3 $1^\circ \times 1^\circ$ aggregation and subsampling algorithm to be better imitated (a non-trivial exercise by any means), it would probably be safe to conclude that subsampling errors should not be a serious concern for individual gridpoints of MODIS D3 (daily) data that have undergone moderate additional temporal averaging ($\sim 2\%$ error for monthly values of mean optical thickness and $\sim 3\%$ for mean effective radius), or for spatial averages such as zonal averages ($\sim 0.5\%$ and $\sim 2.5\%$ for means of optical thickness and effective radius, respectively). Still, a study of the type shown here, but with a global dataset from successive orbits spanning over a month or longer, and which would perhaps examine other SDSs as well, would give a more definitive answer on the impact of MODIS Level-3 subsampling.

Acknowledgements: This work was supported by NASA grant NAG5-11631. The author would like to thank Tamas Várnai, Alexander Marshak, Steve Platnick and two anonymous reviewers for helpful suggestions and ideas that helped improve upon the original manuscript.

References

- [1] M. D. King, W. P. Menzel, Y. J. Kaufman, D. Tanré, B.-C. Gao, S. Platnick, S. A. Ackerman, L. A. Remer, R. Pincus, and P. A. Hubanks, “Cloud and aerosol properties, precipitable water, and profiles of temperature and water vapor from MODIS”, *IEEE Trans. Geosc. Rem. Sens.*, vol. 41, pp. 442-458, Feb., 2003.
- [2] S. A. Ackerman, K. I. Strabala, W. P. Menzel, R. A. Frey, C. C. Moeller, and L. E. Gumley, “Discriminating clear sky from clouds with MODIS,” *J. Geophys. Res.*, vol. 103, pp. 32 141–32 157, 1998.
- [3] S. Platnick, M. D. King, S. A. Ackerman, W. P. Menzel, B. A. Baum, , J. C. Riédi, and R. A. Frey, “The MODIS cloud products: Algorithms and examples from Terra”, *IEEE Trans. Geosc. Rem. Sens.*, vol. 41, pp. 459-473, Feb., 2003.
- [4] M. Nishihama, R. Wolfe, D. Solomon, F. Patt, J. Blanchette, A. Fleig, and E. Masuoka, *MODIS Level 1A Earth Location: Algorithm Theoretical Basis Document Version 3.0*. Available: http://modis.gsfc.nasa.gov/data/atbd/atbd_mod28_v3.pdf
- [5] L. Oreopoulos, and R. F. Cahalan, “Cloud inhomogeneity from MODIS”, *J. Climate*, submitted for publication.
- [6] H. W. Barker, “A parameterization for computing grid-averaged solar fluxes for inhomogeneous marine boundary layer clouds, part I: methodology and homogeneous biases”, *J. Atmos. Sci.*, vol. 53, pp. 2289-2303, 1996.
- [7] L. Oreopoulos, and R. Davies, “Plane parallel albedo biases from satellite observations. Part II: Parameterizations for bias removal”, *J. Climate*, vol. 11, pp. 933-944, 1998.
- [8] D. S. Wilks, “*Statistical Methods in the Atmospheric Sciences*”, Academic Press. 467pp., 1995.

- [9] R. F. Cahalan, W. Ridgway, W. J. Wiscombe, T. L. Bell and J. B. Snider, “The albedo of fractal stratocumulus clouds”, *J. Atmos. Sci.*, vol. 51, pp. 2434–2455, 1994.
- [10] R. F. Cahalan, “Bounded cascade clouds: Albedo and effective thickness”, *Nonlinear Proc. Geophys.*, vol. 1, pp. 156–167, 1994.

List of figures

Figure 1 Subsampling error in the mean and standard deviation of optical thickness (both in %) for each 110x110 pixel region of our dataset. The numbers in the corners are the percentage of regions with errors falling into each of the four quadrants. Note that there were few regions whose errors fell outside the axis limits ($\pm 50\%$) of this plot.

Figure 2 Subsampling error in CF and χ (both in %) for each 110x110 pixel region of our dataset (top), and subsampling error of χ as a function of the actual (perfectly-sampled) cloud fraction of each region (bottom).

Figure 3 Mean error (in %) for various statistics of optical thickness as a function of cloud fraction. The right ordinate shows the number of 110x110 pixel regions with cloud fraction that falls within each 0.1-width bin (regions with cloud fractions less than 0.1 were omitted).

Figure 4 Mean error (in %) of χ and v_{MLE} for each of the 1000 ensembles of 30- and 10000- 110x110 pixel regions as a function of the mean value of the ensemble obtained with perfect sampling.

Figure 5 Top: Subsampling error range (in %) that contains 95% of the 1000 ensembles each of which is made of the number of 110x110 pixel regions shown in the abscissa; bottom: as in top panel, but for 1000 ensembles of 30 regions of the size shown in the abscissa.

Figure 6 As in Fig. 1, but for effective radius.

Figure 7 As in Fig. 3, but for mean and standard deviation of effective radius.

Figure 8 As in Fig. 4, but for mean and standard deviation of effective radius.

Figure 9 As in Fig. 5, but for mean and standard deviation of effective radius.

Figure 10 As the bottom panel of Fig. 5 (save the cloud fraction), but when histograms from subsampled data are used to reconstruct the optical thickness statistics or inhomogeneity parameters. Top panel shows results when the Level-3 binning for liquid clouds is used, and bottom panel when ice cloud binning is used.

Figure 11 As Fig. 10, but for mean and standard deviation of effective radius.

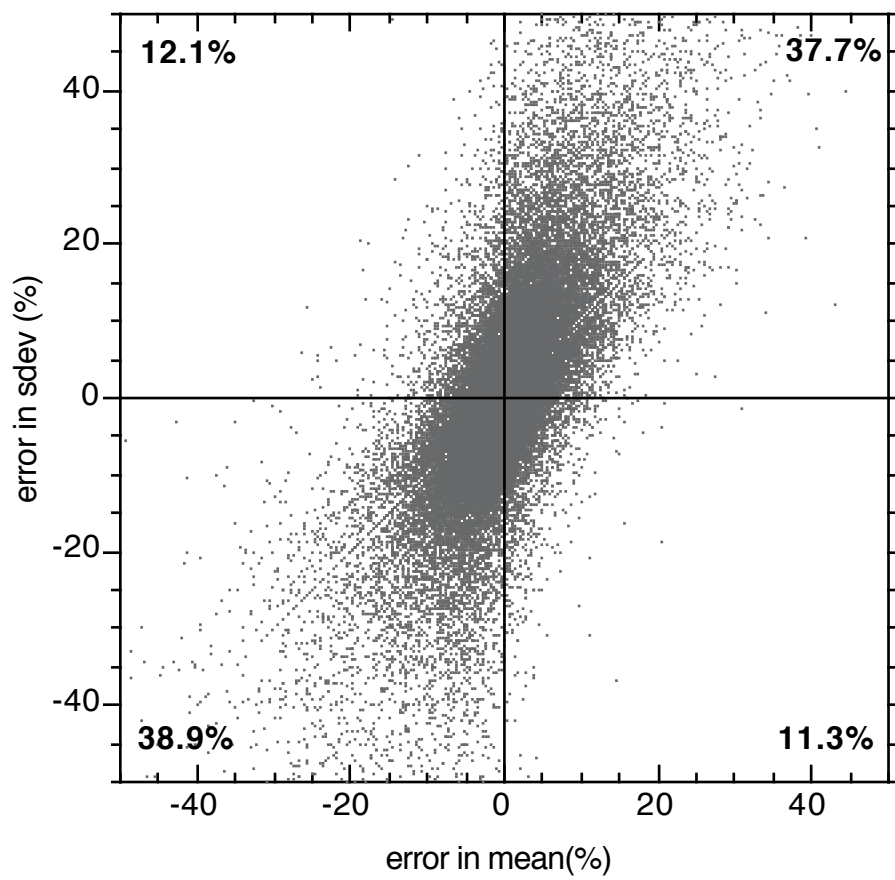


Figure 1

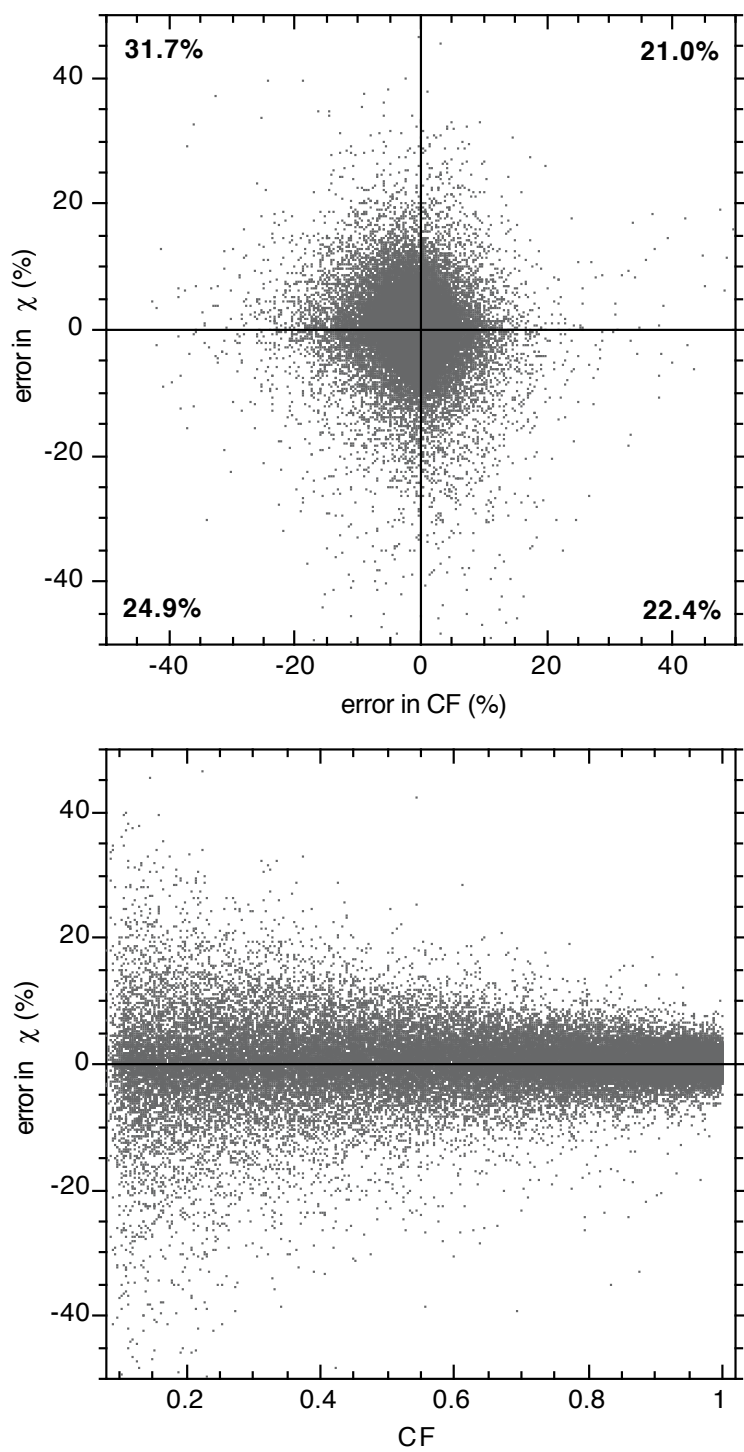


Figure 2

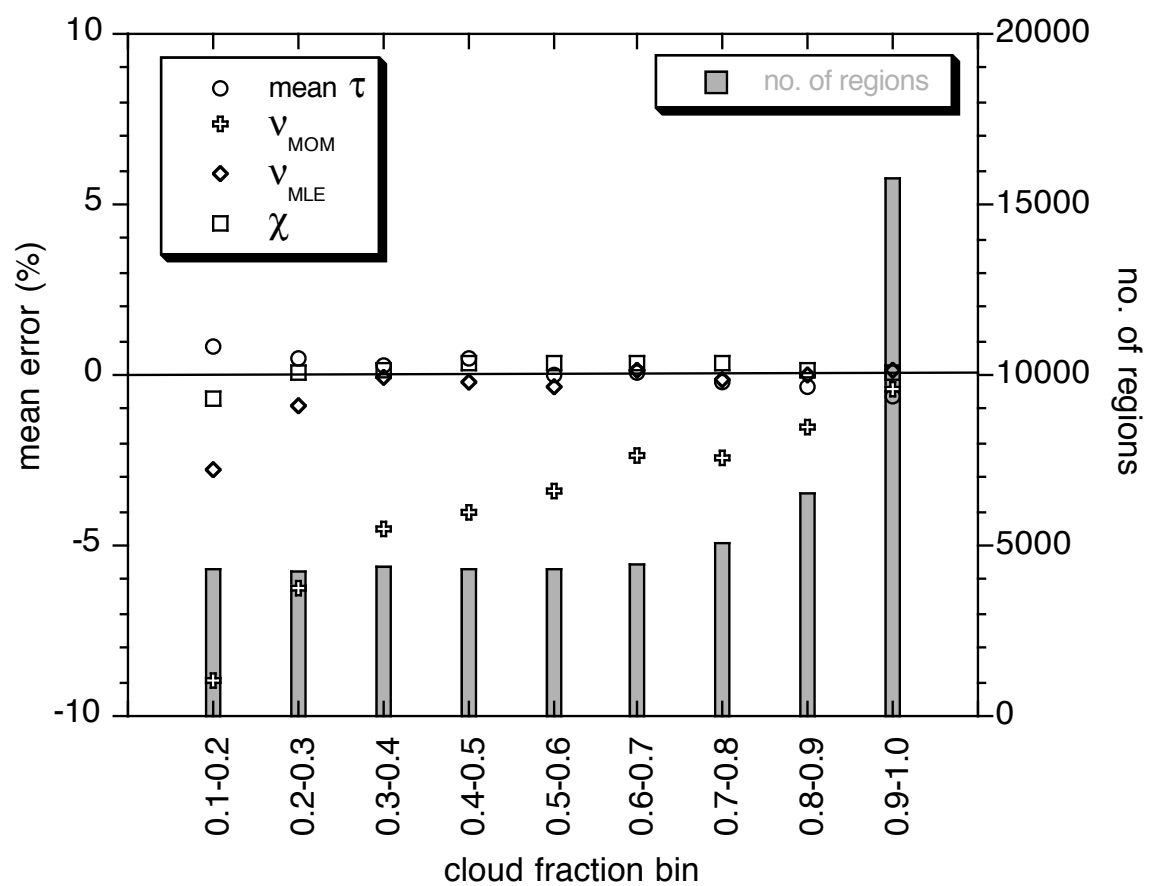


Figure 3

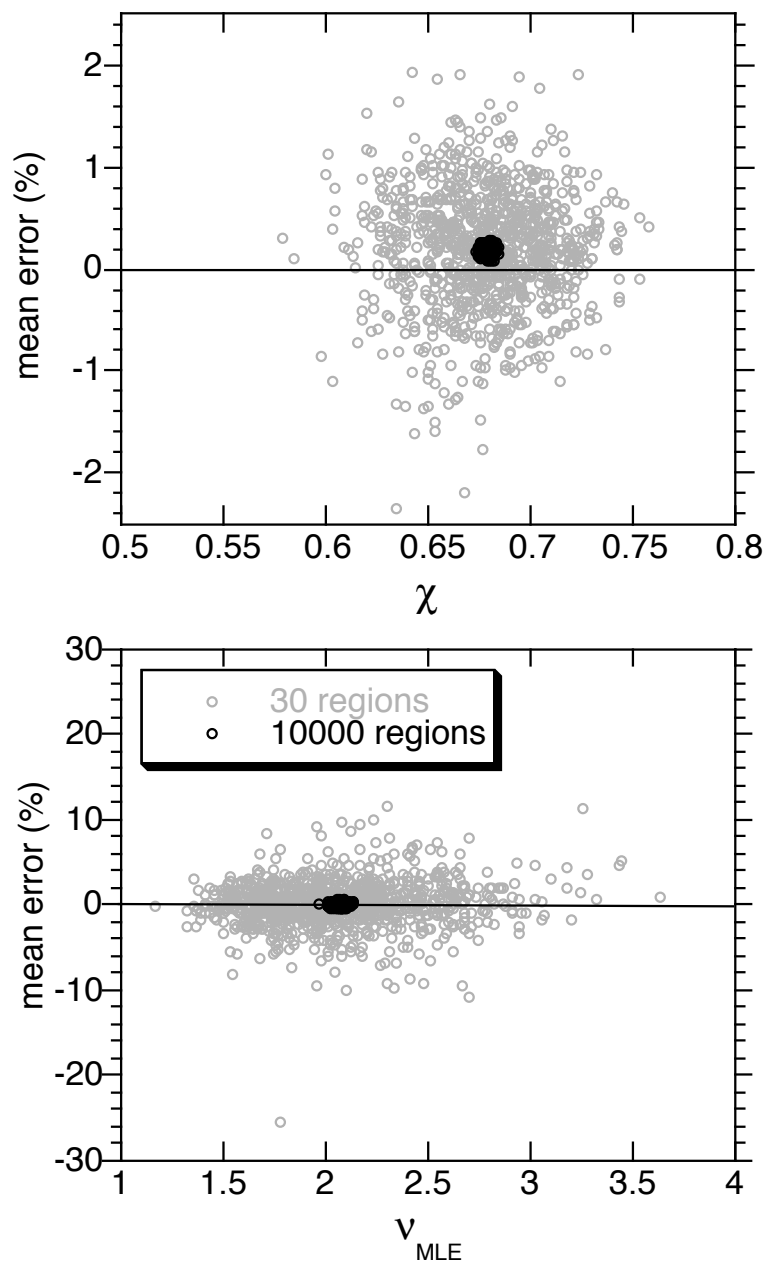


Figure 4

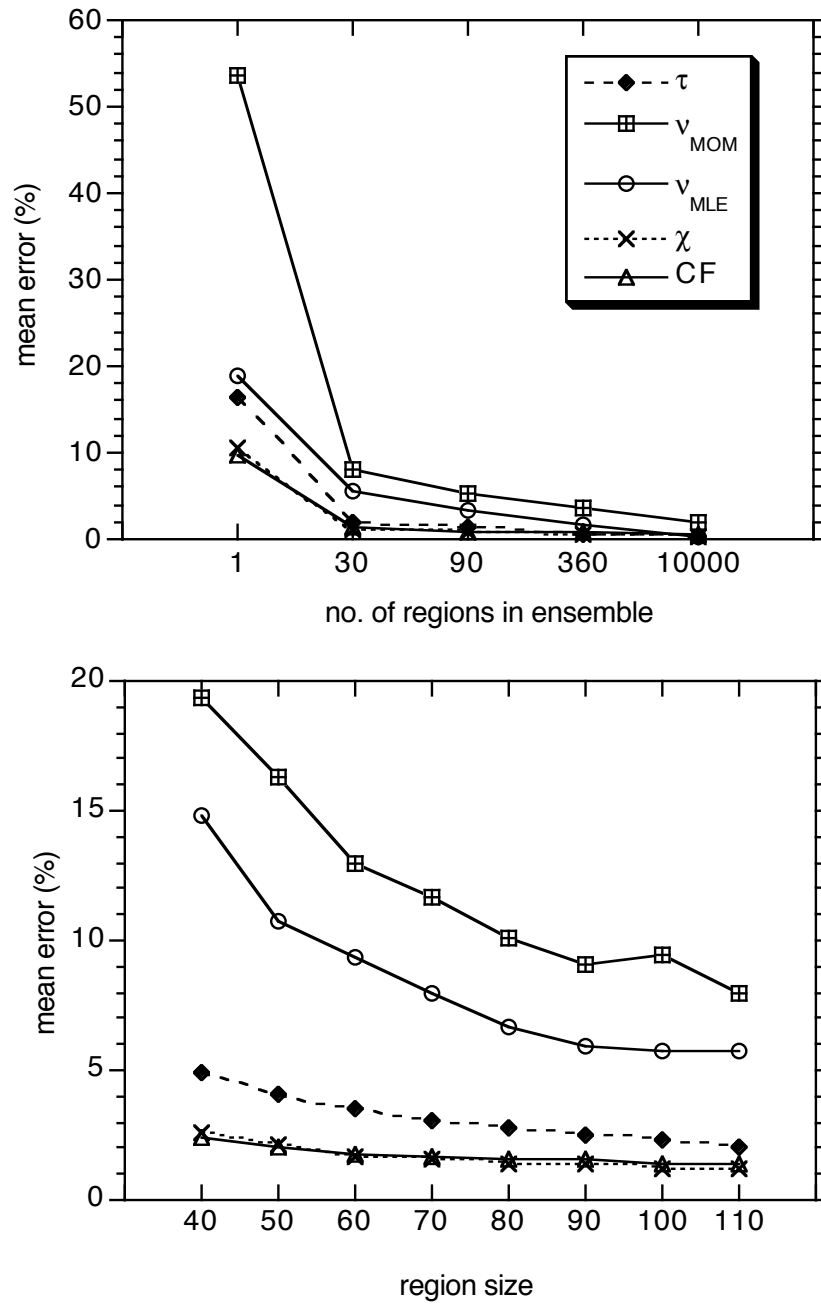


Figure 5

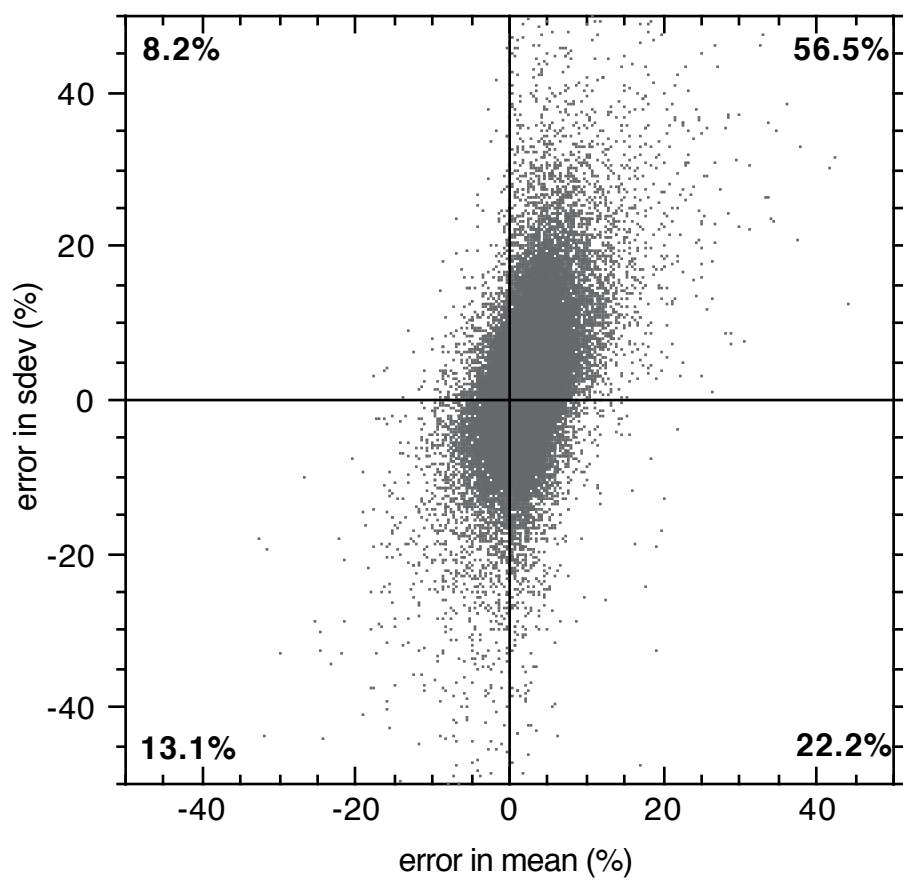


Figure 6

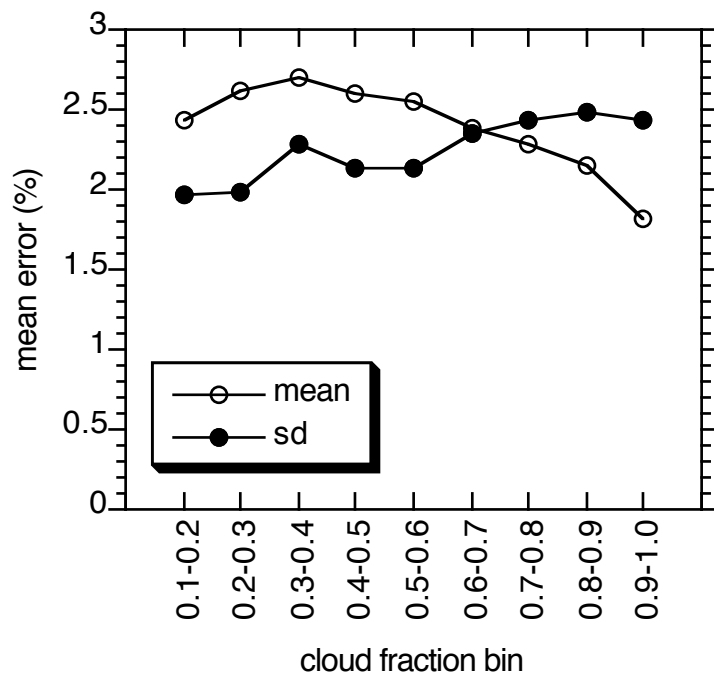


Figure 7

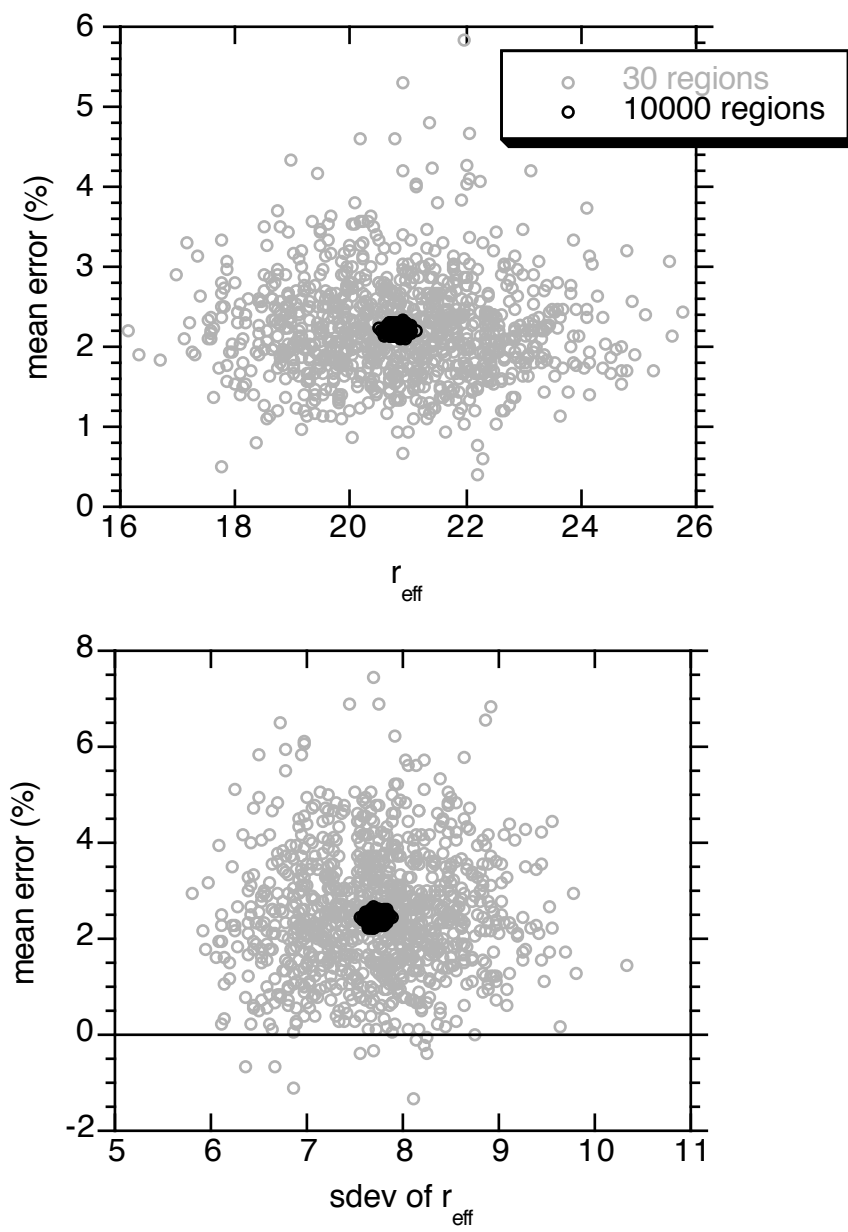


Figure 8

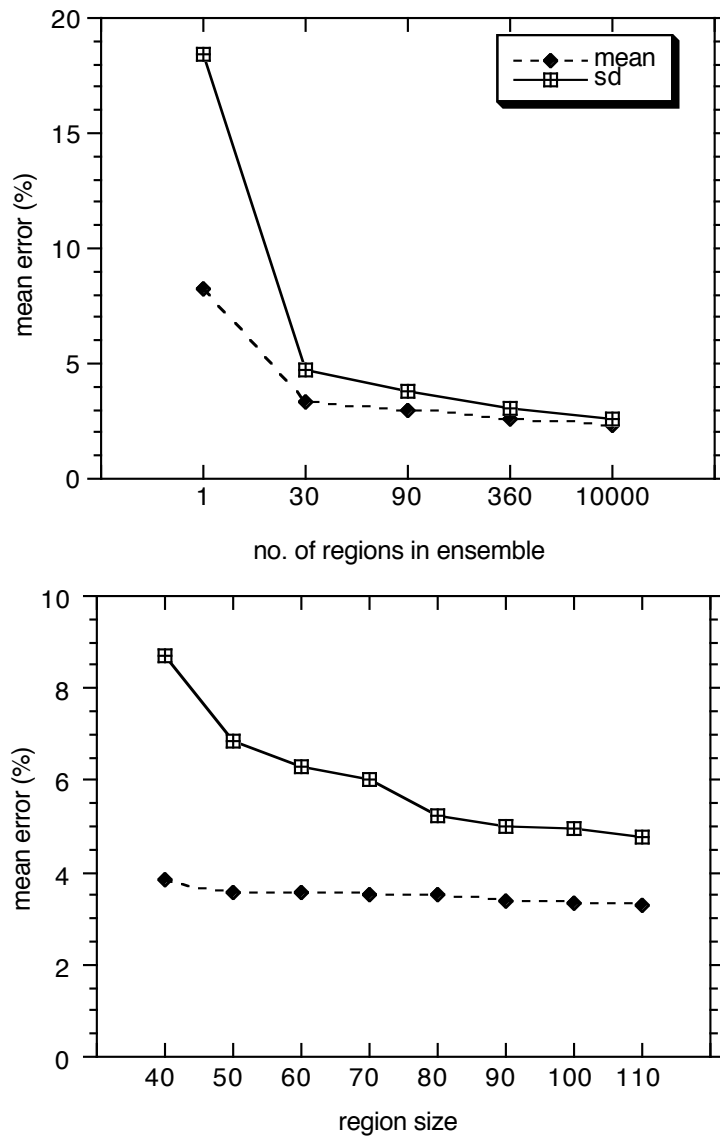


Figure 9

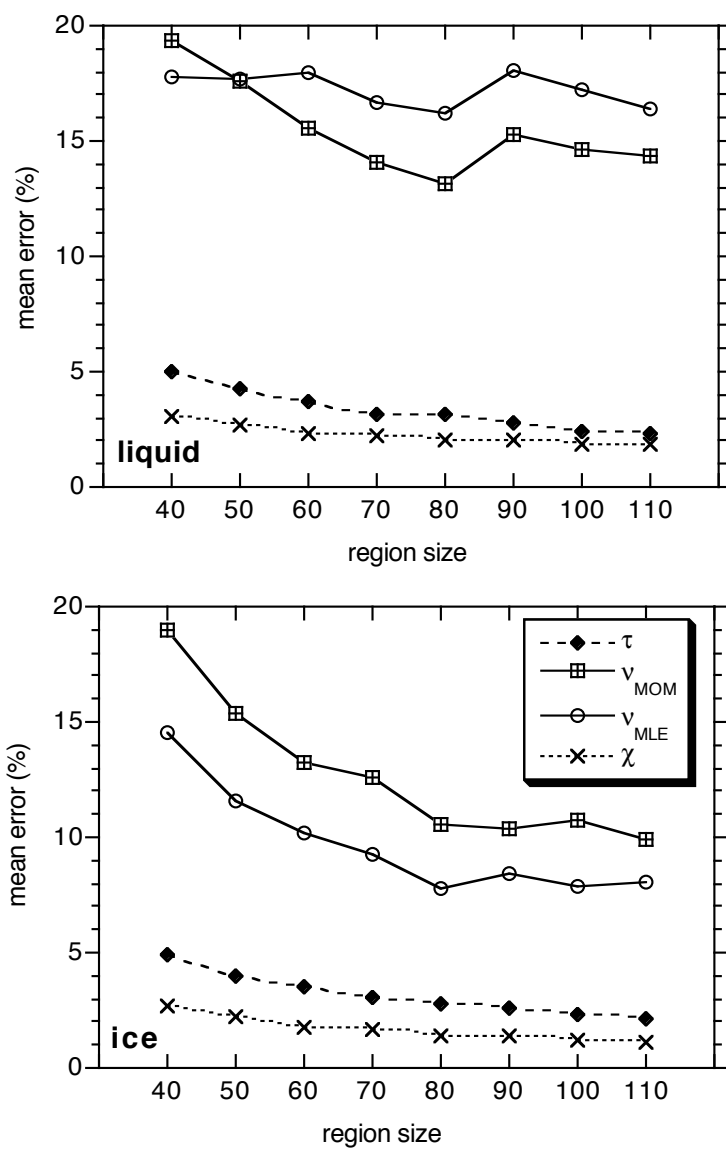


Figure 10

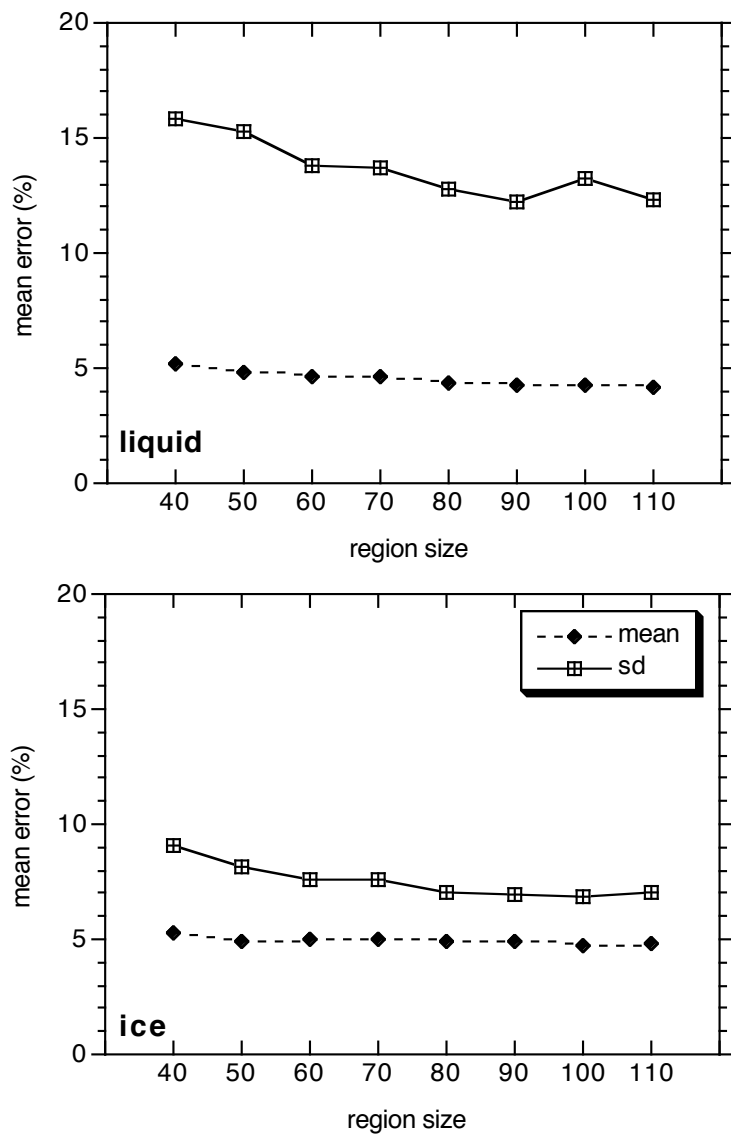


Figure 11